Science of Remote Sensing 6 (2022) 100069

Contents lists available at ScienceDirect

Science of Remote Sensing

journal homepage: www.sciencedirect.com/journal/science-of-remote-sensing

Bias of area counted from sub-pixel map: Origin and correction

Qi Dong [a,b,h], Xuehong Chen [a,b,*], Jin Chen [a,b], Dameng Yin [c], Chishan Zhang [d], Fei Xu [e], Yuhan Rao [f], Miaogen Shen [g], Yang Chen [a,b], Alfred Stein [h]

[a] State Key Laboratory of Remote Sensing Science, Jointly Sponsored by Beijing Normal University and Aerospace Information Research Institute of Chinese Academy of Sciences, Faculty of Geographical Science, Beijing Normal University, Beijing, 100875, China
[b] Beijing Engineering Research Center for Global Land Remote Sensing Products, Institute of Remote Sensing Science and Engineering, Faculty of Geographical Science, Beijing Normal University, Beijing, 100875, China
[c] Institute of Crop Sciences, Chinese Academy of Agricultural Sciences/Key Laboratory of Crop Physiology and Ecology, Ministry of Agriculture, Beijing, 100081, China
[d] Department of Geography and Geographic Information Science, University of Illinois at Urbana-Champaign, Urbana, IL, 61801, USA
[e] Division Forest, Nature and Landscape, KU Leuven, 3001 Heverlee, Leuven, Belgium
[f] North Carolina Institute for Climate Studies, North Carolina State University, Asheville, NC, 28801, USA
[g] Institute of Land Surface System and Sustainable Development, Faculty of Geographical Science, Beijing Normal University, Beijing, 100875, China
[h] Faculty of Geo-information Science and Earth Observation (ITC), University of Twente, Enschede, Netherlands

ARTICLE INFO

Keywords:
Land cover/land use
Sub-pixel mapping
Area bias correction
Small sample size
Abundance-dependent error
Probability distribution of abundances

ABSTRACT

With the increasingly widespread use of sub-pixel mapping techniques in land cover/use mapping, more accurate area information is often required for a specific land cover type in a particular study region. However, the bias of area counted from sub-pixel maps (called area bias below), and the inadequate understanding of the area bias's origin and influential factors pose a challenge to using this information accurately. Traditional model-assisted estimators combining the map and the reference sample showed unreliable performances in the case of small sample sizes collected in target regions. This work presented a theoretical analysis of the origin of area bias. It then proposed a novel bias-adjusted estimator which can effectively deal with the small sample sizes. The theoretical analysis illustrated that area bias mainly originates from two terms, i.e., the abundance-dependent error and the probability distribution of abundances. We next developed a stratified bias-adjusted area estimator named the two-term method (TTM) by incorporating the sub-pixel map and a reference sample obtained from both target and external regions. We validated the effects of different sub-pixel mapping methods, different spatial resolutions, the varying spatial structures of statistical units on area bias, and the performance of TTM in correcting the biased areas in multiple cases. The results showed that area bias varied from zero to approximately 20% with the variation of three influential factors. TTM effectively corrected the biased area values to nearly the true values, showing approximate equivalence with the traditional stratified regression estimator (STRE) when adequate reference samples are collected sorely inside target regions. However, in cases of small samples from target regions, TTM showed significant superiority over STRE in reducing the variance and MSE due to the incorporation of external reference samples. We conclude that the theoretical analysis resulted in a better understanding of area bias counted from sub-pixel maps and an improved area estimator for dealing with the cases of small sample sizes inside target regions.

1. Introduction

Remote sensing has been widely used in land cover/use mapping. Estimating the total area of a specific land cover/use type based upon the mapping results within an administrative or natural unit, such as a municipality or an ecoregion, is an indispensable task for further applications. Commonly, such an area can be counted from either pixel-based maps or sub-pixel maps, obtained by pixel-based mapping (also called hard classification) or sub-pixel mapping (also called soft classification). Pixel-based mapping labels each pixel as a uniform land cover type, while sub-pixel mapping gives an abundance (i.e., proportion) of one land cover type within each pixel.. It should be noticed that sub-

* Corresponding author. State Key Laboratory of Remote Sensing Science, Jointly Sponsored by Beijing Normal University and Aerospace Information Research Institute of Chinese Academy of Sciences, Faculty of Geographical Science, Beijing Normal University, Beijing 100875, China.
E-mail address: chenxuehong@bnu.edu.cn (X. Chen).

https://doi.org/10.1016/j.srs.2022.100069
Received 12 March 2022; Received in revised form 23 July 2022; Accepted 16 September 2022
Available online 17 September 2022

pixel mapping in this article is different from super-resolution mapping which was also often named as sub-pixel mapping in previous literature (Atkinson, 1997; Chen et al., 2018; Wang et al., 2014, 2020; Zhong et al., 2015). For high spatial resolution imagery with almost homogeneous pixels, e.g., Quickbird, WorldView, and airborne data, pixel-based mapping is a dominant technique. For low spatial resolution satellite imagery (i.e., 100 m to 10 km) containing mixed pixels of multiple land cover types, e.g., MODIS and AVHRR, sub-pixel mapping is widely used. And for medium spatial resolution imagery, e.g., Landsat and Sentinel-2, both pixel-based and sub-pixel mapping methods are commonly used depending on different applications (Bullock et al., 2020; Cao et al., 2022; Wu 2004; Xu et al., 2019; Xu and Somers 2021). Both pixel-based mapping and sub-pixel mapping allow one to obtain the area of the target land cover type by pixel counting, i.e., multiplying the pixel size with the number of pixels belonging to the land cover type in a pixel-based map and summing the area of the land cover type within each pixel in a sub-pixel map. However, areas counted from both pixel-based and sub-pixel maps inevitably contain bias (called area bias below).

Area bias in pixel-based mapping has been well recognized (Moody and Woodcock 1994; Ozdogan and Woodcock 2006). It is caused by asymmetric commission/omission classification errors and the coarse spatial resolution of the imagery (Boschetti et al., 2004; Czaplewski 1992; Czaplewski and Catts 1992; Gallego 2004; Waldner and Defourny 2017). Even with accurate land cover maps, area bias may still occur for data with mixed pixels (Ozdogan and Woodcock 2006). In the improvement of area estimation, bias-adjustment area estimators, model-assisted estimators, and stratified estimators were employed by incorporating satellite imagery-derived maps and reference samples (Card 1982; Gallego 2004; Pickens et al., 2020; Stehman 2013; Turubanova et al., 2018). Stehman (2013) explored the relationships among different estimators and recommended stratified estimators for area estimation. From the perspective of the stratified estimator, the reference sample data is the basis for the area estimator, and the classification map provides only the ancillary information for reducing the standard error. In summary, area estimators based upon the reference sample rather than simple pixel counting have been widely considered good practices for estimating area (Olofsson et al., 2014; Stehman and Foody, 2019).

Area bias also exists in sub-pixel mapping. Adhikari and de Beurs (2016) compared a 1 km global cropland percentage map IIASA-IFPRI (Fritz et al., 2015) and a 250 m Global Cropland Extent (Pittman et al., 2010). They showed that the first was in good agreement with the ground truth, while the second showed 56% overestimation at the country level in West Africa. Lobell and Asner (2004) found that wheat areas estimated from MODIS temporal unmixing were closer to their actual areas at units larger than 10 km^2 but biased at smaller units. Although area bias commonly exists in sub-pixel mapping (MacLachlan et al., 2017; Pan et al., 2012), the origin of the area bias attracted inadequate attention. Few studies explored how the area bias is related to multiple influencing factors, though the issue is vital for selecting estimators for improved area estimation and developing superior estimators.

For improving area estimation in the context of sub-pixel mapping, some model-assisted and stratified estimators have been applied in practice (Bullock et al., 2020; King et al., 2017; McRoberts 2010; Potapov et al., 2014; Sannier et al., 2013). Sannier et al. (2013) used a model-assisted regression estimator to estimate forest cover and deforestation areas with a cluster sampling design. Potapov et al. (2014) estimated the area of forest change proportion using a model-assisted ratio estimator with a stratified sampling design. King et al. (2017) constructed a stratified regression estimator and a stratified estimator (i.e., a stratified direct estimator) for national-scale area estimation of soybean in the USA and Argentina, with MODIS-derived abundance defining the strata and Landsat-derived abundance providing the reference sample. They proved that the regression estimator performed better than the stratified estimator in reducing the variance. However, the model-assisted estimators or stratified estimators require an adequate size of sample collected inside the target region to obtain a reliable estimation. In the case of small sample size, the reliabilities of all the model-assisted estimators become questionable because there are possibly no sample units included in one or more strata in the target region (McRoberts 2010; Stehman 2013). In practice, the case of a small sample size is encountered inevitably due to geographical accessibility, budget, and time limitations in the sampling survey. Hence, alternative options for the small sample size must be provided. Compared with the widespread use of model-assisted estimators, the bias-adjusted estimators have not been fully explored in the context of sub-pixel mapping. The bias-adjusted estimator aims to estimate the bias based on the distribution of mapping error, which could be stable across different regions. Thus it is expected to be less dependent upon the sample collected inside the target region and has the potential to provide superior performance over the model-assisted estimators in the case of only a small sample available in the target region.

In summary, there remain the following research gaps on the issue of area bias in sub-pixel mapping: 1) the inadequate understanding of the origin of area bias and how it is related to influencing factors, 2) the lack of exploration of bias-adjusted estimators dealing with the case of a small sample size. Hence, this work first explored the origin of the area bias through theoretical analysis and then proposed a novel bias-adjusted method to correct the biased area counted from the sub-pixel map. Through three experiments, we validated the theoretical analysis of the origin of area bias and its relationships with influencing factors. We furtherly compared our method with a typical model-assisted estimator, stratified regression estimator, in cases of small and large sample sizes, demonstrating the superiority of our method in the case of small sample sizes.

2. Methodology

2.1. Origin of area bias in sub-pixel mapping

Sub-pixel mapping techniques estimate each pixel's abundance of the target land cover type. The estimated abundance of the ith pixel ($\widehat{f}_i$) can be supposed as

$$\widehat{f}_i = f_i + \varepsilon_i, \tag{1}$$

where f_i and ε_i are the true abundance and the corresponding estimation error for the ith pixel. The total area ($\widehat{A}$) of the target land cover type in a study unit counted from the sub-pixel map equals

$$\widehat{A} = r^2 \times \sum_i^N \widehat{f}_i = Z \times \frac{1}{N} \sum_i^N \widehat{f}_i, \tag{2}$$

where r is the pixel size, Z and N are the total area and the total number of pixels of the study unit. As the total area of the unit (Z) is a constant, analysis of the target type area bias is equivalent to analysis of the bias of the target type area proportion (ΔF), which is also the expectation of abundance estimation error ($E(\varepsilon)$).

$$\Delta F = \widehat{F} - F = \frac{1}{N} \sum_i^N \widehat{f}_i - \frac{1}{N} \sum_i^N f_i = \frac{1}{N} \sum_i^N \varepsilon_i = E(\varepsilon), \tag{3}$$

where $\widehat{F}$ and F are the estimated and true area proportion of the target land cover type in the study unit. If the estimation error ε_i is independently and identically distributed, with zero expectation, ΔF approximates zero. However, the abundance estimation error often varies with abundance in reality (Fritz et al., 2015; Hansen et al., 2003; Wu and Murray 2003; Xu et al., 2019)). This error can be decomposed into the part of abundance-dependent error $g(\widehat{f})$ and the part of Gaussian random error ω

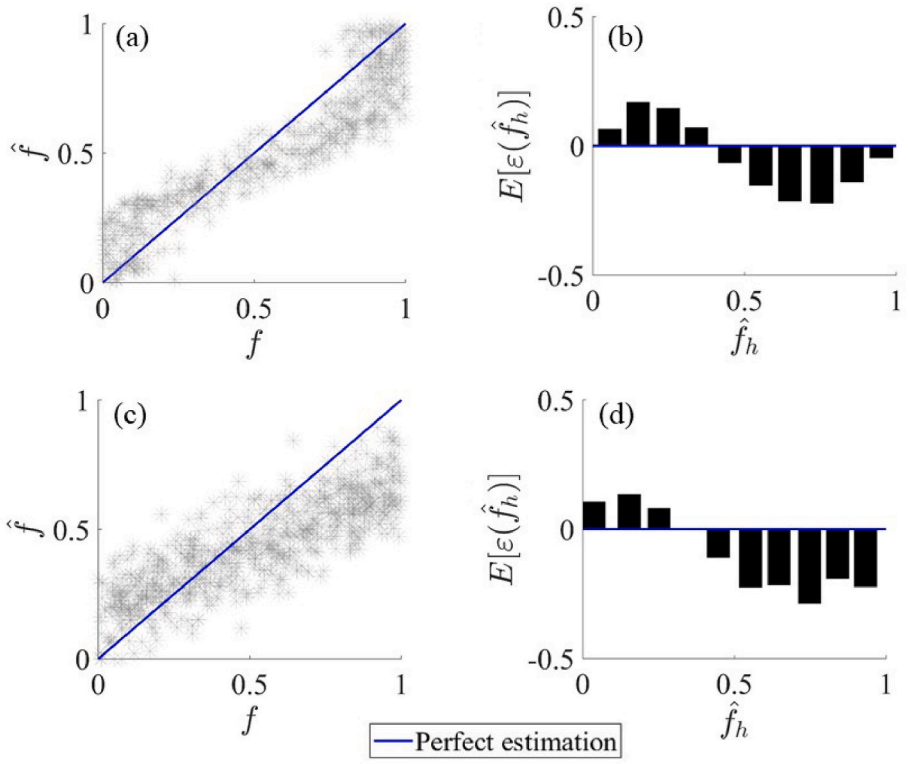

Fig. 1. Conceptive scatter plots of abundance estimation resulted from two typical reasons in sub-pixel mapping (a, c) and the corresponding abundance-dependent error distributions (b, d). The pattern in (a) can result from nonlinear effects commonly existing for index-regression methods and linear spectral mixture analysis (LSMA), and the pattern in (c) can result from additional constraints in sub-pixel mapping techniques such as rules of sum-to-one and zero-to-one in unmixing methods and regularization in machine learning.

$$\varepsilon(\hat{f}) = g(\hat{f}) + \omega, \tag{4}$$

Combining Eqs. (3) and (4), we obtain the bias of the area proportion estimation as the expectation of per-pixel abundance estimation error (ε_i) as the sum of abundance-dependent error at each estimated abundance ($\hat{f}$).

$$\begin{aligned} \Delta F &= \int_0^1 [g(\hat{f}) + \omega] p(\hat{f}) d\hat{f} \\ &= \int_0^1 g(\hat{f}) p(\hat{f}) d\hat{f}, \end{aligned} \tag{5}$$

where $p(\hat{f})$ is the probability distribution of $\hat{f}$. Eq. (5) describes the origin of the area bias in sub-pixel mapping as an interaction effect of abundance-dependent error and the probability distribution of estimated abundance.

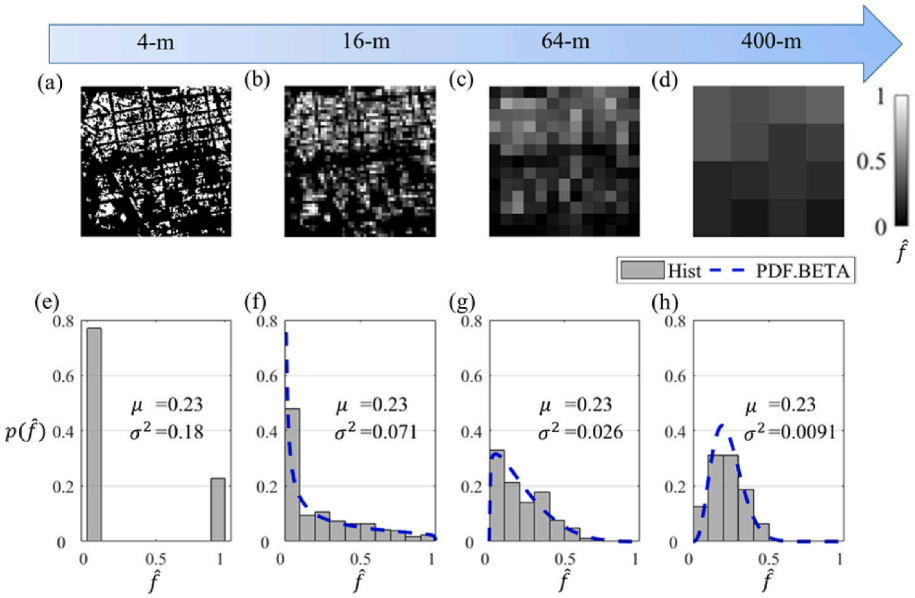

Fig. 2. Abundance maps of one target land cover type (a~d) and probability distributions of abundance (e ~ h) with different spatial resolutions. 'PDF.BETA' means Probability Density Function of the beta distribution.

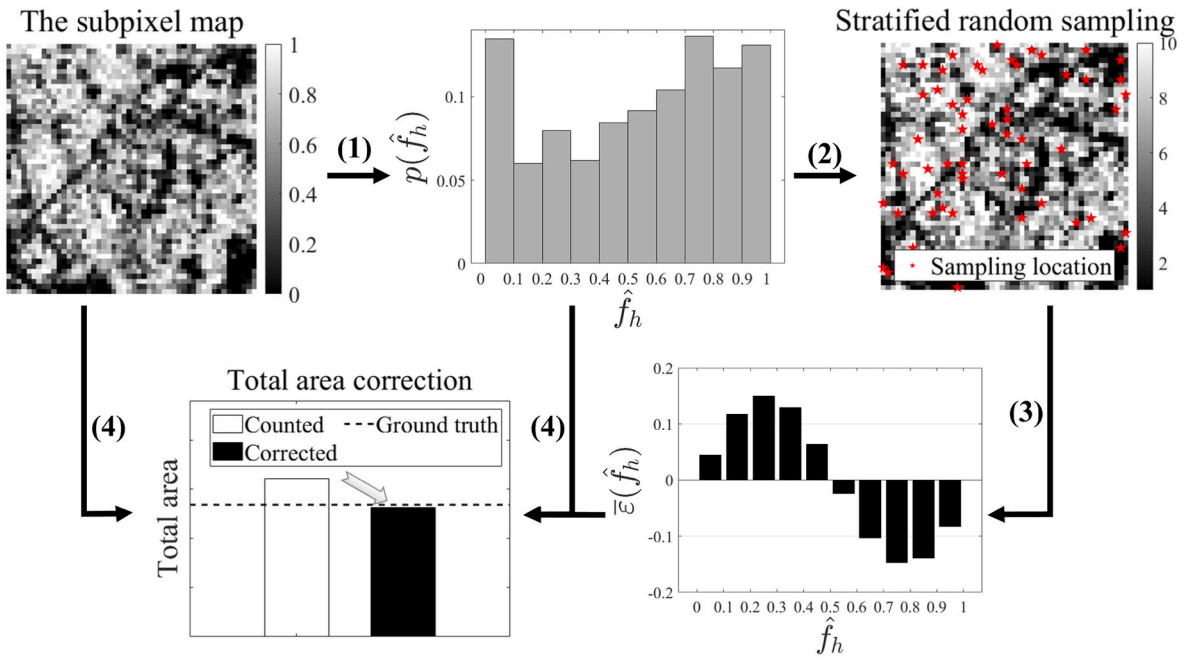

Fig. 3. The flowchart of the proposed two-term method (TTM) for correcting the area estimates counted from sub-pixel mapping results.

2.1.1. *Abundance-dependent error in sub-pixel mapping*

Most sub-pixel mapping methods produce the abundance-dependent error. It mainly results from the inadequate capability of existing sub-pixel mapping methods to deal with the endmember variability and nonlinearity. We distinguish two reasons for this. Firstly, nonlinear effects commonly exist for index-regression methods and linear spectral mixture analysis (LSMA). For example, a vegetation index commonly suffers from the saturation effect, resulting in underestimation bias of high-abundance vegetation pixels (Huete et al. 1997, 2002). LSMA tends to underestimate the fraction of a bright component for a mixed pixel due to the nonlinear spectral mixture induced by the multi-scatter effect (Keshava and Mustard 2002). Such nonlinearities could lead to a nonlinear relationship between estimated abundances and true values (Fig. 1(a). Accordingly, the estimation errors could be distributed dependently on abundances (Fig. 1(b)). Secondly, abundance-dependent error originates from additional constraints in sub-pixel mapping techniques. For example, the spectral unmixing methods derived abundance is often physically constrained by rules of sum-to-one and zero-to-one. Such constraints could result in overestimating low abundance pixels and underestimating high abundance pixels (Roberts et al., 1998) (Fig. 1(c)). Regularization, often used for minimizing overfitting in machine learning, is also a constraint with a cost of estimating bias (Goodfellow et al., 2016). Such regularization would also make machine learning methods overestimate low abundance pixels and underestimate the high abundance pixels (Fig. 1(c)). Accordingly, the distribution of abundance-dependent error like Fig. 1 (d) commonly occurs in sub-pixel mapping results.

2.1.2. *Probability distribution of mixed pixels in a study unit*

The second term in Eq. (5) is the probability distribution of estimated abundance ($p(\widehat{f})$) in a study unit, which varies with different spatial resolutions and structures (Collins and Woodcock 1999). When one specific study unit is observed by satellite sensors with different resolutions, $p(\widehat{f})$ varies as a function of spatial resolution and spatial structure (the overall proportion and fragmentation) of the target land cover type, which can be quantified by the beta distribution with mean (μ) and variance (σ^2) (Collins and Woodcock 1999; Key 1994; Ozdogan and Woodcock 2006). A detailed description of the beta distribution was provided in the appendix. For a specific unit with high overall mapping accuracy, the mean (μ) is approximately a constant, equaling the total area proportion of the target land cover type. In contrast, the variance (σ^2) changes with different resolutions. For example, for a square unit with a target land cover type accounting for 23% of the total area (Fig. 2), with the spatial resolutions of 4-m,16-m,64-m, and 400-m, the means (μ) of pixel abundances all equal 0.23 (Fig. 2(a~d)), while the variance (σ^2) decreases from 0.18 to 0.0091 (Fig. 2(e ~ h)).

In summary, the area bias originates from the interaction between the abovementioned two terms, i.e., the abundance-dependent error and the probability distribution of abundances in a study unit. The two terms are related to three factors: the sub-pixel mapping methods, the spatial resolution of used imagery, and the spatial structure of the target land cover type in the study unit, which are accordingly the influential factors of the area bias.

2.2. *Area estimate correction*

2.2.1. *Regression estimator (RE) and stratified RE (STRE)*

The regression estimator (RE) is a traditional model-assisted estimator which combines a more accurate reference area known for a sample and the commonly biased area known for the whole unit (Gallego 2004). With a simple random sampling design, by using the RE method for estimating the area proportion from sampling and sub-pixel map, the estimated proportion equals

$$F_{\mathrm{RE}} = \overline{f} + b(\widehat{F} - \widehat{\overline{f}}), \tag{6}$$

where $\overline{f}$ and $\widehat{\overline{f}}$ are the mean values of the reference abundance and the mapping abundance for the sample, and $\widehat{F}$ is the total area proportion counted from the sub-pixel map (i.e., the mean abundance of all pixels). b is the ordinary least squares (OLS) regression estimator (i.e., the estimated slope for the regression of reference abundance (f) on estimated abundances ($\widehat{f}$)). When b is a constant not depending on the sample data, e.g., $b = 1$, the regression estimator is equivalent to the difference estimator (Gallego 2004; Stehman 2013). RE considers the reference abundance of the sample as the basic information, and the mean value of sampling reference abundance is compensated with the difference of estimation abundance between the sample and the population.

RE could be simply extended as a stratified version (i.e., STRE) as:

$$F_{\mathrm{STRE}} = \frac{1}{N}\sum_{h}^{L} N_h\left(\bar{f}_h + b_h(\hat{F}_h - \hat{\bar{f}}_h)\right), \tag{7}$$

where N is the population size (i.e., the number of pixels) of the target region, L is the number of strata, N_h is the population size of stratum h, $\bar{f}_h$ and $\hat{\bar{f}}_h$ are the mean values of the reference and mapping abundance for the sample, respectively. $\hat{F}_h$ is the total area proportion of stratum h counted from the sub-pixel map (i.e., the mean abundance of all pixels in stratum h), b_h is the OLS regression estimator for stratum h. When b_h is fixed to 1, STRE is equivalent to the stratified difference estimator (STDE). When b_h is flexibly computed without the constraint of equaling 1, the STRE is expected to have a smaller variance than the STDE, especially for the low overall mapping accuracy where b_h has a large discrepancy from 1 (Stehman 2013). With the estimated abundance groups as strata, the sample can be divided into more homogeneous subgroups, reducing the estimator's variance. STRE is always more efficient than RE if the sample has an adequate size for stratification. In the case of a small sample size for the target region, however, no sample units could be included in one or more strata, resulting in low reliability of STRE.

2.2.2. A two-term method (TTM)

Based on the theoretical analysis of the origin of area bias in Section 2.1, we proposed a new area estimate method named the two-term method (TTM). Unlike the regression estimator, TTM is a bias-adjusted estimator that focuses on estimating the area bias instead of directly estimating the area proportion. According to Eq. (5), the area bias can be estimated if $g(\hat{f})$ and $p(\hat{f})$ are obtained. TTM method consists of four steps, as shown in Fig. 3. Firstly, the term $p(\hat{f})$ is directly acquired from the sub-pixel map by histogram analysis with a specific interval $\Delta\hat{f}$; secondly, a stratified random sampling survey is conducted to collect the ground truth abundances in each stratum (i.e., each bin in the histogram), denoted as $\hat{f}_h \in [\hat{f}, \hat{f}+\Delta\hat{f}]$ for stratum h; thirdly, the term $g(\hat{f})$ of each stratum is approximated as the mean error of the sample ($\bar{\varepsilon}(\hat{f}_h)$); and fourthly, the area proportion bias ($\Delta\hat{F}$) obtained by Eq. (5) is approximated as:

$$\Delta\hat{F} = \sum_{h}^{L} \bar{\varepsilon}(\hat{f}_h)p(\hat{f}_h), \tag{8}$$

where L is the total number of strata, $\bar{\varepsilon}(\hat{f}_h)$ is the mean error of the sample in stratum h, and $p(\hat{f}_h)$ is the probability of stratum h accounting for the whole unit. With the estimated area bias, the area proportion can be corrected as

$$\begin{aligned} F_{\mathrm{TTM}} &= \hat{F} - \Delta\hat{F} \\ &= \hat{F} - \sum_{h}^{L} \bar{\varepsilon}(\hat{f}_h)p(\hat{f}_h), \end{aligned} \tag{9}$$

where F_{TTM} is the corrected area proportion by TTM, which is expected to approach the true area proportion more. And the total area could also be calculated by multiplying by the area of the study unit (Z).

For the stratification step in TTM, we constructed ten strata with $\Delta\hat{f} = 0.1$ ($\hat{f}$ falling in 0–0.1, 0.1–0.2, …, and 0.9–1.0). Considering the ease of implementation, efficiency, and cost, proportional allocation (Cochran 1977) is employed and each sample unit is a single pixel. It should be noted that TTM assumes that the first term (the abundance-dependent error) shares high similarity across different regions if the identical mapping technique is implemented. Accordingly, the first term for the target region can be obtained from external sample units. Therefore, TTM has the potential to provide reliable area estimates even in the case of small sample size by incorporating external sample units outside the target region.

2.2.3. Comparison between uncertainties of TTM and STRE

For the assessment of area estimators, the uncertainty composed of unbiasedness and sampling variability should be present. Sampling variability of an estimator refers to the degree to which the sample-based estimate would vary over different realizations of the sampling survey (Stehman 2009). Both TTM and STRE estimate the area by combing the sub-pixel map and reference sample. The critical difference between them is the potential source of the reference sample. For STRE, the reference sample is required to be collected inside the target region, while for TTM, the reference sample can be collected inside or outside the target region. Such a difference results from the different contributions of the reference sample in the two methods.

Based on stratified random sampling inside the target regions (Cochran 1977, p.92, Eq. (5.6)), STRE produces approximately unbiased estimates with the mean value equaling the true area value F, and the variance (King et al., 2017) equaling

$$V(F_{\mathrm{STRE}}) = \sum_{h=1}^{L} W_h^2\left(\frac{1}{n_h} - \frac{1}{N_h}\right)\left(S_{f_h}^2 - 2b_h S_{\widehat{ff}_h} + b_h^2 S_{\widehat{f}_h}^2\right), \tag{10}$$

where $W_h = N_h/N$ is stratum weight; n_h is the sample size for stratum h; $S_{f_h}^2$ and $S_{\widehat{f}_h}^2$ are the sample variances of f and $\hat{f}$ in stratum h, and $S_{\widehat{ff}_h}$ is the sample covariance between $\hat{f}$ and f in stratum h. As STRE is approximately unbiased, the MSE of STRE equals the variance estimated by Eq. (10) as:

$$MSE(F_{\mathrm{STRE}}) = V(F_{\mathrm{STRE}}). \tag{11}$$

TTM is equivalent to STRE with b fixed to 1 if the sample units are all inside the target regions. Compared with the flexible b_h-based STRE which can better fit the reference and map data, TTM may have a slightly larger variance than STRE with an identical adequate sample size in target regions. However, the variance of TTM could be reduced by introducing external sample units outside the target regions as:

$$\begin{aligned} V(F_{\mathrm{TTM}}) &= \sum_{h=1}^{L} W_h^2\left(\frac{1}{n_H} - \frac{1}{N_h}\right)S_H^2 \\ &\sum_{h=1}^{L} W_h^2\left(\frac{1}{n_H} - \frac{1}{N_h}\right)\left(S_{f_H}^2 - 2S_{\widehat{ff}_H} + S_{\widehat{f}_H}^2\right), \end{aligned} \tag{12}$$

where n_H is the sample size of stratum H, including the sample size inside and outside the target region; $S_{f_H}^2$ and $S_{\widehat{f}_H}^2$ are the sample variances of f and $\hat{f}$ in stratum H; and $S_{\widehat{ff}_H}$ is the sample covariance between $\hat{f}$ and f in stratum H. Therefore, the variance of TTM estimate could still keep a low value when the sample units in the target regions are inadequate. However, the mean of TTM results can be biased from the true value because of the slight difference in abundance-dependent error among target and external regions:

$$Bias(F_{TTM}) = \sum_{h}^{L} \Delta\bar{\varepsilon}(\hat{f}_h)p(\hat{f}_h), \tag{13}$$

where $\Delta\bar{\varepsilon}(\hat{f}_h)$ is the difference in the abundance-dependent error of stratum h between the target and external regions. And the MSE of TTM includes both bias and variance:

$$MSE(F_{\mathrm{TTM}}) = Bias^2(F_{\mathrm{TTM}}) + V(F_{\mathrm{TTM}}). \tag{14}$$

with the increased sample size from external regions, TTM is expected to have a smaller variance but risk a larger bias than STRE. The difference in MSE between the two methods depends upon the trade-off between

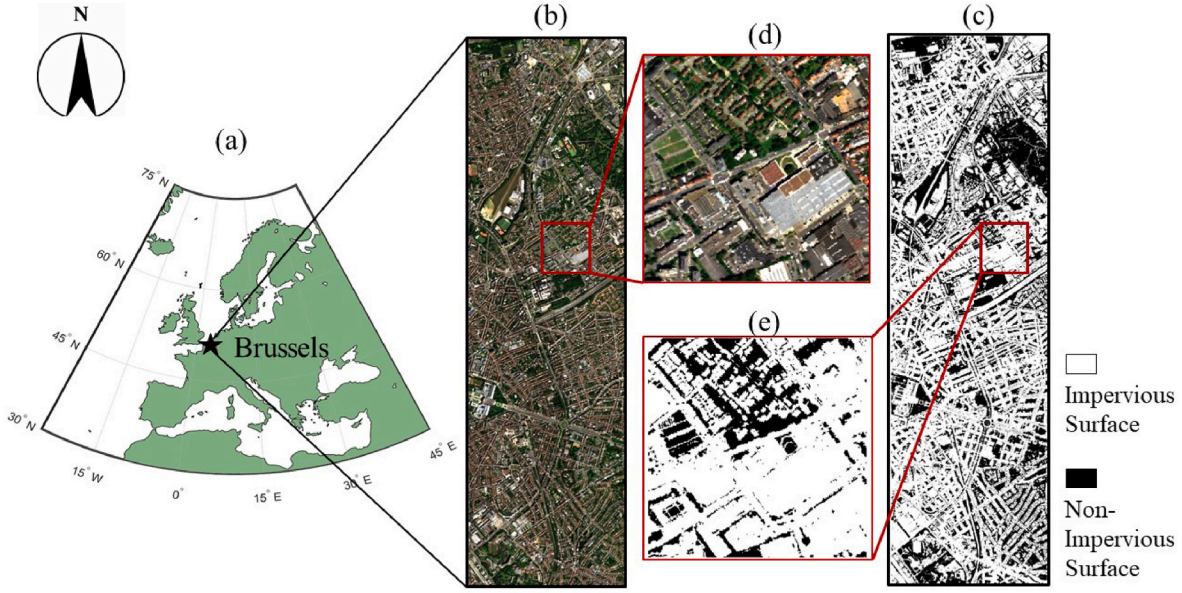

Fig. 4. The geographic location of the study region in EXP I (a) and the land surface composition (b ~ e). (b) and (c) are the true color composite image and the impervious surface map with 2 m resolution of the study region. (d) and (e)showed the spatial details of (b) and (c). (For interpretation of the references to color in this figure legend, the reader is referred to the Web version of this article.)

the two components and the discrepancy of b_h from 1 in STRE. Our expectation is as follows: in the case of a large sample for the target region, STRE has a smaller MSE. In the case of a smaller sample for the target region, TTM has a smaller MSE. Hence, incorporating sample units from external regions and implementing TTM can be a superior option for a small sample size.

3. Validation experiments

Three experiments were conducted to validate the theoretical analysis of the origin of area bias and the performance of the proposed area-adjusted estimator TTM for different sample sizes. In practical applications, sub-pixel maps can be produced using different sub-pixel mapping methods, with remotely sensed data of different spatial resolutions, and for study regions with different spatial structures. The three factors impact the area bias, hence we conducted three experiments (EXP I, EXP II, and EXP III) to test the impact of the three factors on area bias and then validate the theoretical analysis on understanding the origin of area bias. We varied one of the three factors in each experiment while keeping the other two fixed for sub-pixel mapping. TTM and STRE were then applied to correct the counted areas. In EXP I and II, adequate samples were collected inside the target region, and TTM is equivalent to STDE (i.e., STRE with constraining b_h to 1) and slightly different from STRE with a flexible b_h. In EXP III, the samples for STRE were inside the target regions, but the samples for TTM were from both the target and external regions. In this case, the two estimators are inequivalent, and their uncertainties were compared for different sample sizes. The sampling survey and area estimation process was repeatedly conducted 500 times. To better support the validation, the repeated sampling survey processes in the three experiments are all simulations based on high-resolution imagery-derived reference maps instead of real field surveys or visual interpretation. Then, the 500 corrected area estimates' mean and variance were calculated to evaluate the uncertainty.

3.1. EXP I: scenario of varying sub-pixel mapping methods

Experiment I aimed to validate the theoretical analysis of the effect of sub-pixel mapping methods on area bias and to evaluate TTM in cases of different sub-pixel mapping methods. Spatial monitoring of impervious surface abundances (ISA) with sub-pixel mapping techniques is an important part of land cover science (Deng and Wu 2012; Powell et al., 2007; Ridd 1995; Weng 2012; Wu 2004; Zha et al., 2003). In particular, the spectral variability of impervious surfaces challenges sub-pixel mapping techniques and results in inevitable area bias (Somers et al., 2011; Zare and Ho 2014; Zhang et al., 2019)), which provide an appropriate opportunity to conduct this experiment.

The study region is located in 4.3914–4.4179°E, 50.8188–50.8820°N and covers the eastern part of the Brussels Capital Region, Belgium (Fig. 4), which is mainly composed of three land cover types, i.e., impervious surface accounting for 66% and vegetation/soil occupying

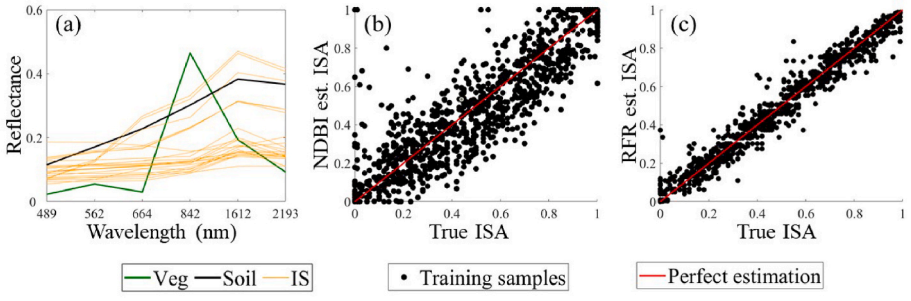

Fig. 5. The inputting parameters/training performances of three sub-pixel mapping methods for ISA mapping. Endmember spectral library of MESMA method (a), the good consistency between the ground truth and estimated ISA of the training sample by the NDBI- regression model(b) and RFR (c).

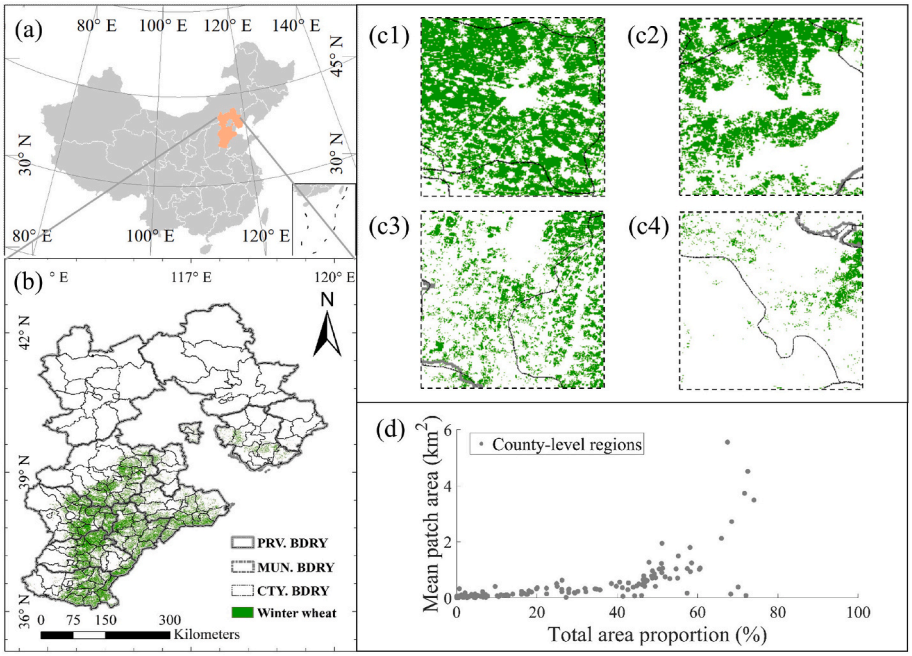

Fig. 6. The geographic location of Hebei province in China (a), the map of sub-level administrative units (municipal-level and county-level units) and the reference map of winter wheat (b), four representative spatial structures of winter wheat cropland (c1-c4), the distribution of total area and mean patch size of winter wheat cropland in the 167 county-level units (d).

the rest. Using an APEX (Airborne Prism Experiment) sensor boarded on an airplane operating at an altitude of 3600 m. a.s.l., a hyperspectral image with 2 m and 218 spectral bands (450–2350 nm) covering the study region was acquired on June 30, 2015. By spectrally resampling, an image with 2 m and six bands of 489 nm (blue), 562 nm (green), 664 nm (red), 842 nm (NIR), 1612 nm (SWIR1), and 2193 nm (SWIR2) was obtained (marked as "spectrally resampled hyperspectral image - SRH image" in following paragraphs). By applying the SVM classifier to the SRH image, we obtained a 2 m resolution land cover map of the study region (with an overall classification accuracy of 90%) as a ground truth map. Meanwhile, we resampled the 2 m resolution SRH image and ground truth map to obtain the 20 m reflectance image with six bands and the reference ISA map.

Three typical methods were selected for mapping ISA at a 20 m sub-pixel scale over the study region: Multiple Endmember Spectral Mixture Analysis (MESMA) (Roberts et al., 1998), Normalized Difference Built-up Index (NDBI) (Zha et al., 2003) -based regression and Random Forest Regression (RFR) (Breiman 2001).

In MESMA, multiple candidate endmembers (i.e., representative reflectance spectra of different land covers of interest) were input into a linear spectral mixing model. The abundance value was obtained with the optimal solution with a minimal model fitting error. Practically, we visually interpreted the 2 m SRH image and selected 23 impervious surface reflectance spectra and two vegetation and soil spectra (Fig. 5 (a)) as input for MESMA.

In NDBI-based regression, NDBI is calculated as

$$\mathrm{NDBI} = \frac{\rho_{SWIR1} - \rho_{NIR}}{\rho_{SWIR1} + \rho_{NIR}}, \tag{15}$$

where ρ_{SWIR1} is the reflectance of the shortwave infrared band (1612 nm) and ρ_{NIR} is the reflectance of the near-infrared band (842 nm). NDBI is sensitive to impervious surface spectra and has been widely used to detect impervious surface distributions by remote sensing (Hu et al., 2016; Zhang et al., 2009). We first built a linear regression model of ISA versus NDBI values using the training sample with 1000 pixels. Then, the estimated ISA is constrained into 0–1 (Fig. 5(b)).

Random Forest Regression (RFR) model is also a widely applied approach for land cover sub-pixel mapping. The training sample (pixel reflectance spectra versus ISA) in the NDBI regression model also served to build the RFR model. In the process of training the RFR model, we fine-tuned the hyperparameters (i.e., ntree = 1000 and mtry = 2) in RStudio (Breiman 2002) and obtained a satisfactory model (Fig. 5(c)).

For the area estimation using TTM and STRE, the sampling sizes for each sub-pixel map were determined with the error tolerance of area proportion equaling 0.01 with the 95% confidence level, using a proportional allocation (Cochran 1977, p.105, Eq. (5.48)).

3.2. EXP II: scenario of varying spatial resolutions

Experiment II aimed to validate the theoretical analysis of the effect of spatial resolution on area bias and evaluate TTM in cases of remotely sensed data with different spatial resolutions. In the same study area as EXP I (Fig. 4) and using the MESMA method with identical parameters as in EXP I, ISA maps were produced with the reflectance images of 10 m, 20 m, 30 m, 60 m, 100 m, 200 m, and 500 m resampled from the 2 m SRH image by pixel aggregation. The reference ISA maps with corresponding spatial resolutions were also aggregated from the 2 m ground truth ISA map. For the area estimation using TTM and STRE, the sampling sizes for each sub-pixel map were determined with the error tolerance of area proportion equaling 0.01 with the 95% confidence level, using a proportional allocation (Cochran 1977, p.105, Eq. (5.48)).

3.3. EXP III: scenario of varying spatial structures of statistical units

Experiment III was designed to validate the theoretical analysis of the effect of spatial structure on area bias and evaluate TTM in cases of varying spatial structures and different sample sizes. Agricultural statistics of crop planting areas in administrative units or agricultural zones are essential for the agricultural economy and decision-making. Here we aimed to obtain the cultivated areas of wheat in 167 county-level administrative units of Hebei province, China. A 16 m winter wheat map of 2013–2014 produced from GF-1 data served as the ground truth for high classification accuracy (overall accuracy of higher than 85%) and high spatial resolution (Tang et al., 2016) (Fig. 6(b)). The 167

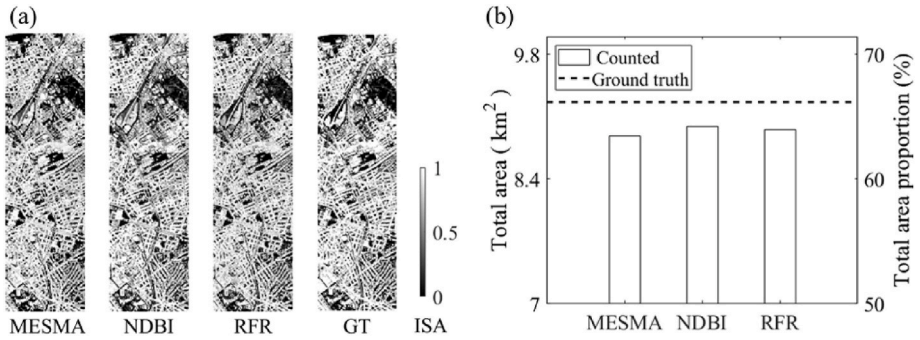

Fig. 7. The 20 m ISA maps produced by MESMA, NDBI-regression, and RFR, and the ground truth (GT) ISA map (a), the counted total areas of impervious surfaces with deviations from the ground truth value (b).

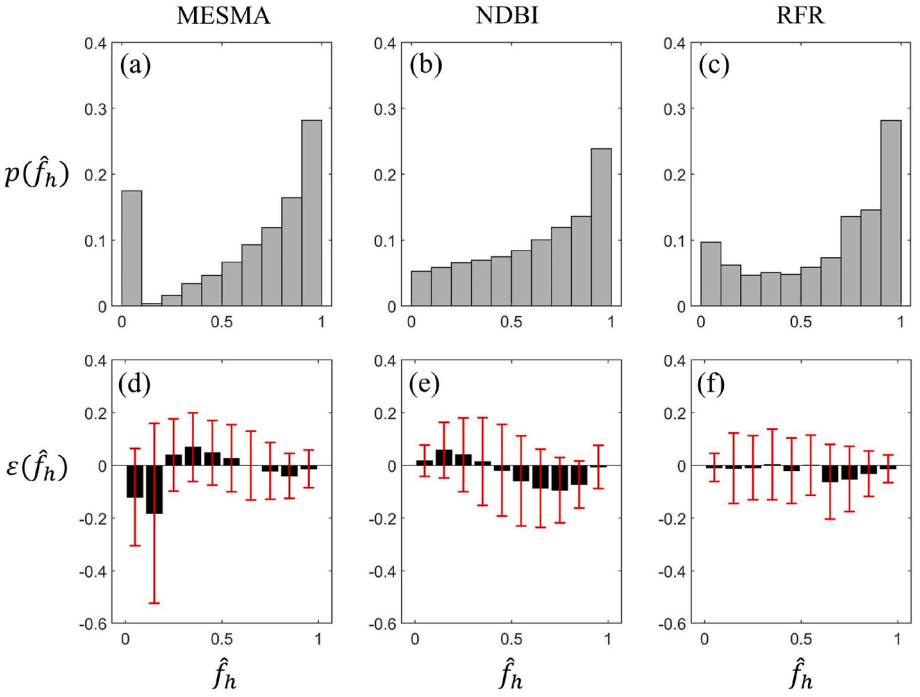

Fig. 8. The probability distributions of estimated abundances (a~c), the abundance-dependent error (black bars), and Gaussian errors (red error lines) of (d ~ f) of MESMA, NDBI-regression, and RFR method. (For interpretation of the references to color in this figure legend, the reader is referred to the Web version of this article.)

county-level units have noticeably different spatial structures of winter wheat cultivation (see four examples in Fig. 6(c1~c4)), with the total area proportions and the mean patch areas varying from 0 to 80% and from 0.0096 km^2 to 5.56 km^2 (Fig. 6(d)).

We produced a 250 m winter wheat abundance map of the whole province based on 16-day MODIS-EVI time-series data (MOD13Q1) from 2013 to 2014 and by using a Crop Phenology Proportion Index (CPPI) method (Pan et al., 2012). One hundred pixels were collected around the province to train the five regression coefficients of CPPI. With the 250 m map, the total areas of winter wheat in 167 counties were counted and then corrected using TTM and STRE. For evaluating the performances of TTM and STRE for different sample sizes, the sample size was set to 500, 1000, 2000, 4000, and 6000 pixels. For the implementation of TTM, samples were collected across all the regions (i.e., the whole province) and used for calculating the first term, i.e., the abundance-dependent error. Then the term was shared for each individual region (i.e., county) for area correction. For the implementation of STRE, the total sample size was averagely allocated to each county. Accordingly, the sample size for each county is 3, 6, 12, 24, and 36 pixels. The area estimates were individually calculated using the collected samples inside each county.

4. Results

4.1. EXP I results

Counted from the 20 m ISA maps generated by MESMA, NDBI-regression, and RFR methods (Fig. 7(a)), the total areas of impervious surfaces showed an underestimation of 2.687%, 1.966%, and 2.232% (Fig. 7(b)), respectively.

The probability distributions of estimated abundances (Fig. 8(a~c)) and the abundance-dependent error and Gaussian error (Fig. 8(d ~ f)) were calculated from the population (i.e., all the pixels) for each bin of $\Delta f = 0.1$. Among the three methods, the probability distributions of abundances showed a similar pattern in high abundances (i.e., larger than 0.5) while noticeable differences in low abundances (i.e., lower than 0.5). The abundance-dependent error also showed patterns with similar underestimation in high abundances and the differences in low abundances. Consequently, the underestimation magnitude varied among the three mapping methods. The counted area from NDBI

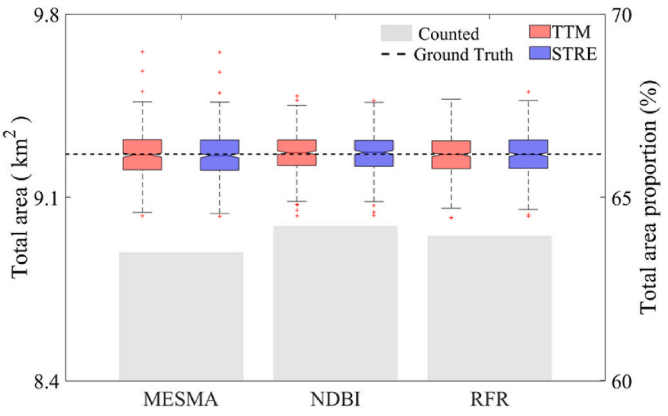

Fig. 9. The total area estimates of the impervious surface before and after correction by using TTM and STRE for three sub-pixel mapping methods. The gray bars represent the counted areas, and the boxplots in red and blue are the distributions of 500 repeated area estimates corrected by TTM and STRE, respectively. (For interpretation of the references to color in this figure legend, the reader is referred to the Web version of this article.)

regression-based map has the slightest discrepancy to the true value, though the abundance-dependent error is larger than that of RFR. This result is due to the more significant canceling effect of over- and under-estimation error among strata of the NDBI-derived map, validating the theoretical analysis of the effect of the sub-pixel mapping method on area bias.

The 500 area estimates derived by TTM and STRE were computed and compared with the true value (Fig. 9). The mean area estimates of both TTM and STRE approach closely to the true value, confirming that both methods are unbiased estimators in this case. For TTM and STRE, the uncertainties (equaling 1.96 standard deviations) of corrected areas were 1.17% vs. 1.18%, 1.05% vs. 1.04%, 1.09% vs. 1.11% for three sub-pixel mapping methods, which satisfied the pre-defined error tolerance (1% with 95% confidence level). TTM is almost equivalent to STRE in this experiment because they used identical samples collected inside the target region.

4.2. EXP II results

Counted from the ISA maps with coarsening spatial resolution, the underestimation of the counted area decreased from −3.0720% to −0.3473% (Fig. 10). Because the probability distribution of estimated abundance became more concentrated (i.e. smaller variance in Eq. (A2)) when the spatial resolution coarsened (Fig. 11(a)); correspondingly, there was a decreasing number of pixels with low abundance, which had the high abundance-dependent error (Fig. 11(b)) and resulted in smaller area bias. This experiment validated the analysis that the area bias is affected by spatial resolution and showed how it is affected. For a fixed target region, the coarser spatial resolution makes the probability distribution of abundances more concentrated in the total area. Accordingly, the area bias will be determined more by the abundance error at the corresponding stratum.

Similar to the results of EXP I, TTM and STRE produced approximately equivalent estimates, of which the mean values are unbiased from the true values, and the variances of TTM and STRE estimates (ranging from 0.5685% to 1.1290% and from 0.5659% to 1.1272%, respectively) meet the defined 1% tolerance (Fig. 12, Table 1).

4.3. EXP III results

The produced 250 m winter wheat abundance map of Hebei province (Fig. 13(a)) showed an overall spatial distribution generally consistent with the 16 m ground truth map (Fig. 13(b)), except for the significant inconsistency in the northeastern part.

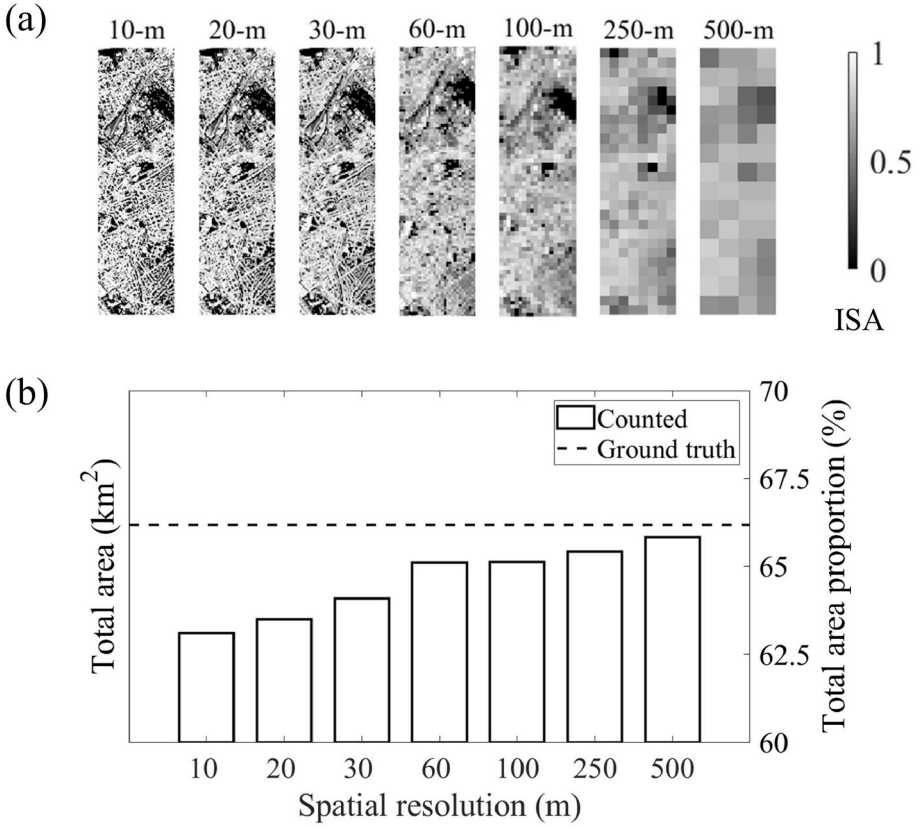

Fig. 10. The derived ISA maps with different spatial resolutions (a) and the counted area estimates (b).

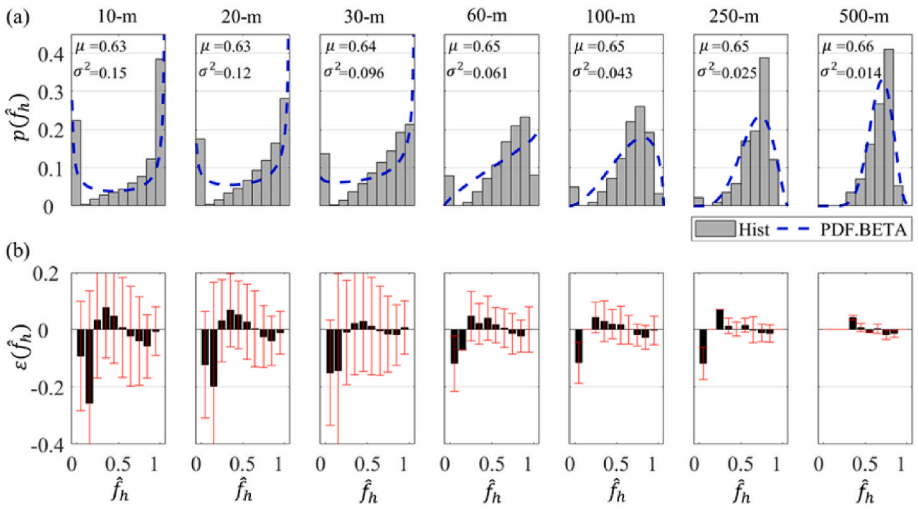

Fig. 11. The probability distributions of estimated ISA (a), the abundance-dependent error (black bars), and Gaussian errors (red error lines) of estimated ISA (b) with different spatial resolutions. The dashed blue lines in (a) are the probability density functions (PDF) of beta distributions fitted with the means and variances of histograms. (For interpretation of the references to color in this figure legend, the reader is referred to the Web version of this article.)

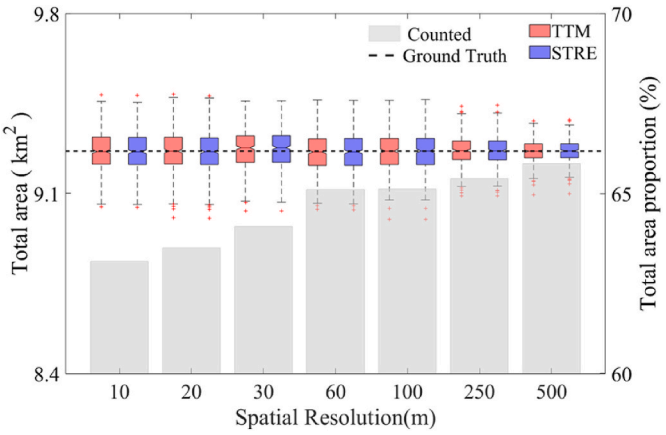

Fig. 12. The area estimates of the impervious surface before and after correction by using TTM and STRE with different spatial resolutions. The gray bars represent the counted areas, and the boxplots in red and blue are the distributions of 500 repeated area estimates corrected by TTM and STRE. (For interpretation of the references to color in this figure legend, the reader is referred to the Web version of this article.)

The relationship between the counted winter wheat areas and the corresponding ground truth values for all the 167 county-level administrative units was calculated (Fig. 15(a)), exhibiting different bias magnitudes for different units. As the abundance-dependent error showed a similar sinusoidal-like pattern for the whole province (Fig. 14 (a)), the difference in the area bias was mainly influenced by the probability distribution of estimated abundance. The area bias showed a decreasing trend with increasing the μ and σ of $p(\hat{f}_h)$ (Fig. 14(f)). It is because the sinusoidal-like pattern of abundance-dependent error could counteract each other when distributed in a wide range (i.e., large σ).

The winter wheat area estimates derived by TTM and STRE with different sample sizes were compared (Table 2, Fig. 15(b–e)) in the 167 counties-averaged MSE, bias, and standard deviation. Compared with the ground truth values, both TTM and STRE corrected the biased areas to a large extent, whereas the uncertainties of TTM of STRE showed differences with different sample sizes. STRE-derived area estimates always showed negligible biases because it is approximately unbiased theoretically. TTM had larger biases than STRE, but the variances of TTM were significantly smaller than those of STRE. As the sum of bias^2 and variance, smaller MSE values were produced by TTM for smaller sample sizes (1000 and 2000 pixels) while by STRE for larger sample sizes (4000 and 6000 pixels). The larger biases of TTM resulted from a uniform abundance-dependent error for all of the statistical units instead of individual ones, which can be slightly different among units (see four examples in Fig. 14 (b ~ e)). But the incorporated external sample sizes effectively reduced the variances and resulted in the reduction of MSE

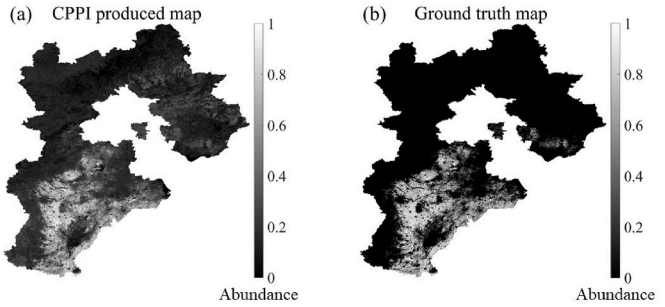

Fig. 13. The produced 250 m winter wheat abundance map (a) and the 16 m ground truth map (b) of Hebei province, China.

Table 1
The 500 repetitions-based uncertainties of impervious surface area estimates before and after correction using TTM and STRE with different spatial resolutions in EXP II.

		10 m	20 m	30 m	60 m	100 m	250 m	500 m
Counted Bias(%)		−3.0720	−2.6876	−2.0968	−1.0664	−1.0526	−0.7652	−0.3473
TTM	Bias(%)	−0.0140	−0.0221	−0.0346	−0.0076	0.01806	0.02315	−0.0022
	95%CI(%)	1.0421	1.1290	1.0261	0.9725	0.9799	0.8484	0.5685
STRE	Bias (%)	−0.0255	−0.0331	−0.0344	−0.0078	0.0180	0.0210	−0.0024
	95%CI(%)	1.0406	1.1272	1.0258	0.9754	0.9803	0.8581	0.5659

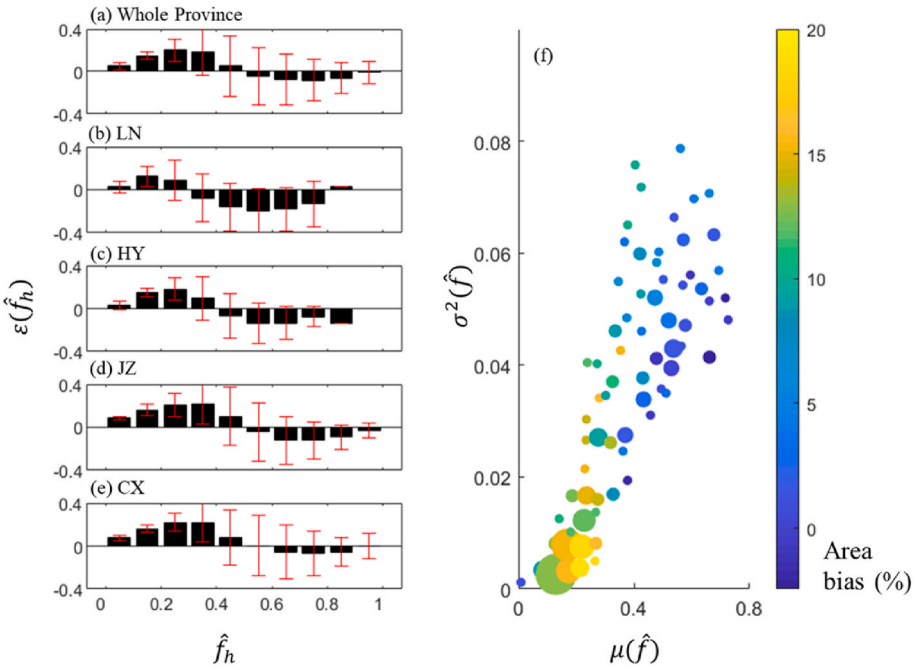

Fig. 14. The abundance-dependent error (black bars) and Gaussian error (red error lines) of winter wheat abundance for (a) the whole province and four county-level administrative units (b) Luannan county, (c) Huangye city, (d) Jinzhou city, and (e) Cixian County. The relationship between the winter wheat area bias and the probability distribution parameters of estimated abundance (the mean $\mu(\hat{f})$ and variance $\sigma^2(\hat{f})$) for all the county-level administrative units (f). (For interpretation of the references to color in this figure legend, the reader is referred to the Web version of this article.)

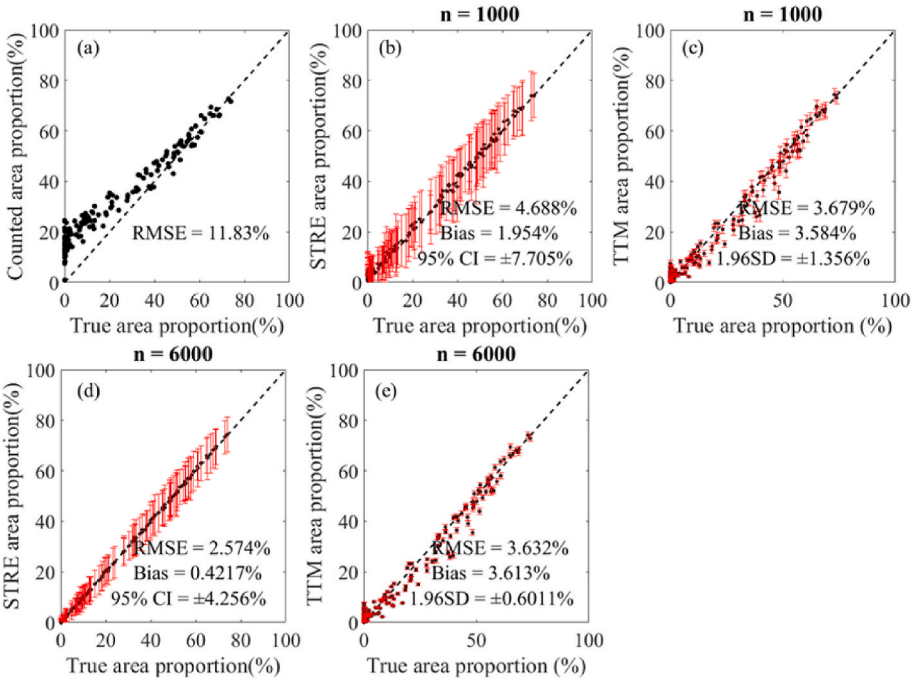

Fig. 15. The relationship between the ground truth and estimated area proportions of winter wheat before (a) and after correction by using STRE (b, d) and TTM (c, e) using 1000 and 6000 reference sample pixels, respectively. Each scattering point represents a county. The dashed line is the perfect estimation (1:1) line, and the black dots and red error bars in (b, c, d, e) represent the mean estimated areas and 1.96 standard deviations (95% confidence intervals for STRE) of 500 repetitions. (For interpretation of the references to color in this figure legend, the reader is referred to the Web version of this article.)

Table 2
Winter wheat area proportion estimates uncertainties (%) of 500 repetitions derived by STRE and TTM with different sample sizes in EXP III.

		Sample size			
		1000	2000	4000	6000
MSE (%)	STRE	4.688	4.274	3.275	2.574
	TTM	3.679	3.665	3.674	3.632
Bias (%)	STRE	1.954	1.3	0.6124	0.422
	TTM	3.584	3.618	3.651	3.613
95%CI(%) 1.96SD (%)	STRE	7.705	7.131	5.35	4.256
	TTM	1.356	0.948	0.6826	0.601

values with TTM for small sample sizes. The results validated the expectation that TTM incorporating external sample units has superiority over STRE in case of small sample size, despite the biased estimates.

5. Discussion

5.1. Variance versus bias in sub-pixel mapping techniques

When assessing sub-pixel mapping techniques, the mean squared error (MSE) of pixel-based abundance (i.e. MSE = Variance + Bias^2) is widely used. Our theoretical analysis revealed that the two

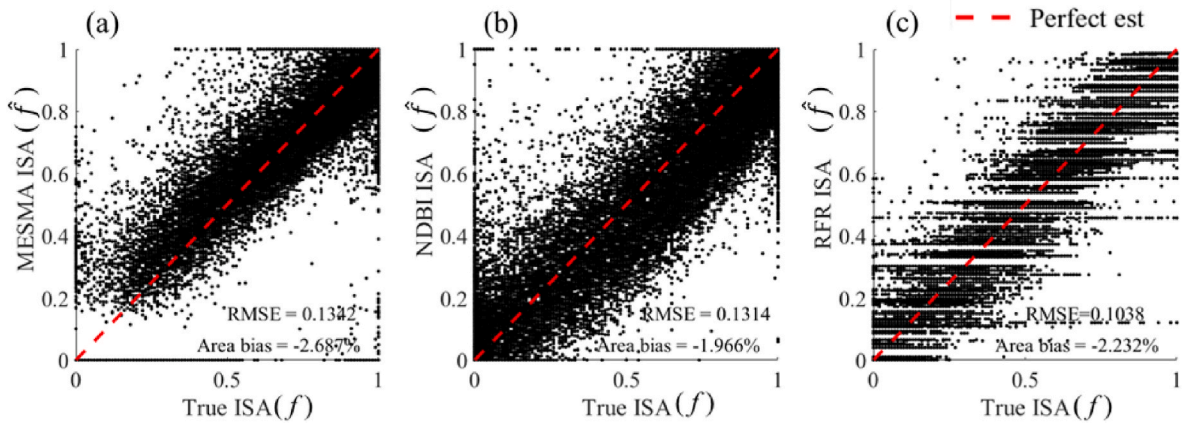

Fig. 16. The relationship between the true abundance and estimated abundance derived by three sub-pixel mapping methods (a) MESMA, (b) NDBI regression, and (c) Random forest regression in EXP I. Each scattering point represents a pixel, and the red dashed line represents the perfect estimation (1:1) line. (For interpretation of the references to color in this figure legend, the reader is referred to the Web version of this article.)

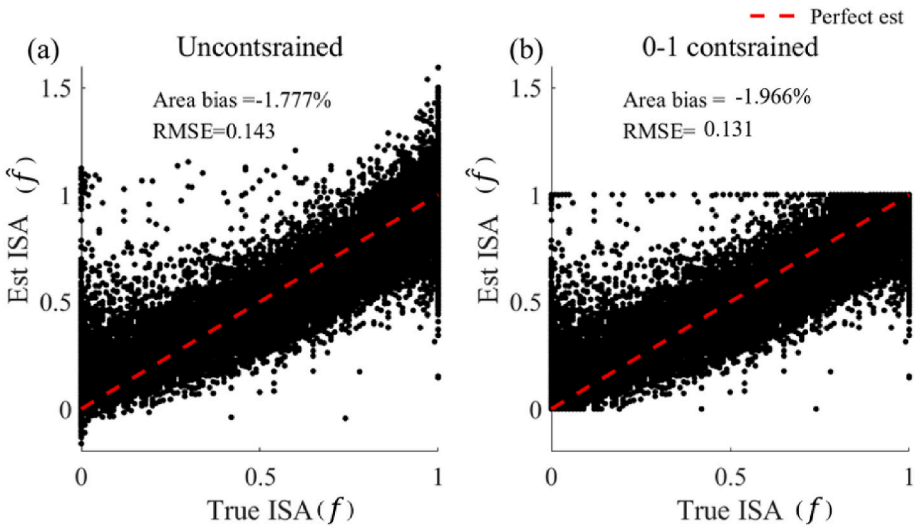

Fig. 17. The relationship between the true and estimated ISA derived by using unconstrained (a) and 0–1 constrained (b) NDBI regression methods in EXP I. Each scattering point represents a pixel, and the red dashed line is the perfect estimation (1:1) line. (For interpretation of the references to color in this figure legend, the reader is referred to the Web version of this article.)

components of MSE have different contributions to the total area bias in a statistical unit. Among a large number of pixels, the variance component can offset to nearly zero and thus has a more negligible contribution to the total area bias. The bias component, however, makes a higher contribution to the total area bias and is hardly negligible. Therefore, even a low MSE of abundance may result in a large bias of total area if the MSE contains a large bias. One example is EXP I, where the RFR method has a smaller MSE (0.1038) than the NDBI regression method (0.1314); however, the area counted from the map derived by RFR had a larger bias than that by NDBI (Fig. 16).

Another example is the comparison between constrained-NDBI and unconstrained-NDBI regression methods (the estimated value is not constrained into the range of 0–1). We noted that the bias of counted area for the former (−1.966%) is larger than that of the latter (−1.777%), despite the lower RMSE (0.1314) of the former compared with the latter (0.143) (Fig. 17). Unfortunately, previous efforts on improving sub-pixel mapping aimed to reduce the MSE rather than the bias. This study recommends that techniques with smaller bias should be used to reduce area bias, even if the variance of abundance and MSE may increase. As the tradeoff between bias and variance correspond to the tradeoff between under-fitting and over-fitting in machine learning (Goodfellow et al., 2016), regularization in machine-learning methods should be reconsidered when using it for area estimation.

5.2. *TTM versus STRE*

From the perspective of practical application, the critical difference between TTM and STRE is the source of the reference sample. External sample units can be incorporated in TTM. In contrast, only internal sample units are used in STRE. From the perspective of understanding, such a difference is in the role of the sub-pixel map in area estimation. In our derivation, TTM is considered as a bias-adjusted estimator for compensating the bias of the area counted from the sub-pixel map (Eq. (9)), where sub-pixel maps provide basic information for area estimation. However, STRE is a model-assisted estimator considering the reference sample as the basis of area estimation and incorporating the sub-pixel map as the auxiliary information (Gallego 2004; Stehman 2013).

One superiority of TTM over STRE is that the introduced external sample has the potential to support an increased number of strata and accordingly produce a reduced variance. With a stratified random sampling design inside the target region, the sample sizes of some strata

are too small or even zero. In this case, a poststratified estimator (i.e., applying a stratified estimator to data obtained from a simple random sample) is more recommended (Stehman 2013). For example, a post-stratified regression estimator was used for 1000 and 2000 sample pixels in EXP III. However, a poststratified regression estimator still produced larger variances and MSE values than TTM, which incorporated external samples. Consequently, TTM is more recommended than a stratified or poststratified regression estimator for cases of small sample sizes in target regions. Regarding determining the strata number with the interval $\Delta\widehat{f}$ when implementing TTM, ten strata were defined with $\Delta\widehat{f}$ equaling 0.1 in the analysis and experiments. However, users can adjust the strata number according to the available sample size. When the sample size is small, the strata number should be reduced to avoid lacking sample units in some strata.

5.3. Limitation of this work

One shortcoming of TTM is the risk of biased estimations, which depends on the $\Delta\bar{\varepsilon}(\widehat{f}_h)$ in Eq. (13), i.e., the difference in the abundance-dependent error of stratum h between the target and external regions. Selecting TTM or model-assisted estimators should be determined by comparing Eqs. (11) and (14), which is related to both the sample size and the bias term. The bias term could be related to the sub-pixel mapping methods and the utilized remote sensing imagery, but how to accurately estimate this term needs to be explored in future research. Another limitation concerns the theoretical analysis of the origin of area bias. Apart from the three influential factors considered in section 2.1, the effect of sensors' point spread functions (PSF) can change the value of the true area and result in possible area bias, which is slight in most cases but sometimes can be significant (Wang et al., 2020). Taking a parcel (i.e., an aggregation of pixels) instead of a pixel as a sample unit can help reduce the PSF effect to some extent, and how to further reduce such effect on area estimation using multi-sensor data should be explored in future.

6. Conclusion

Sub-pixel mapping for area estimation plays an increasingly important role in land cover science, especially at large spatial scales or in long-term historical periods. This work analyzed the origin of area bias in sub-pixel mapping and developed a novel bias-adjusted area estimator named TTM for correcting the biased area. The theoretical analysis helped better understand the area bias concerning three influential factors. Despite the risk of bias, TTM can obtain improved area estimates than traditional model-assisted estimators for small sample sizes due to incorporating an external sample. Consequently, TTM is recommended for improving area estimates counted from sub-pixel maps for small sample sizes in target regions, such as in land cover mapping of large areas or long-term historical periods.

Declaration of competing interest

The authors declare that they have no known competing financial interests or personal relationships that could have appeared to influence the work reported in this paper.

Acknowledgments

This study is supported by the National Natural Science Foundation of China (No. 41871224). Besides, the authors would like to thank the help given by Prof. Ben Somers of KU Leuven for providing the APEX data.

Appendix

The function $p(f)$ varying as a function of spatial resolution and spatial structure of the target land cover type can be quantified by the beta distribution as

$$p(f,\alpha,\beta)=\frac{\Gamma(\alpha+\beta)}{\Gamma(\alpha)\Gamma(\beta)}f^{\alpha-1}(1-f)^{\beta-1},\quad 0<f<1, \tag{A1}$$

where Γ represents the Gamma function, α andβ are two parameters defining the beta pdf, and both are related to the mean (μ) and variance (σ^2) of the distribution as

$$\beta=\frac{1-\mu}{\sigma^2}\left[\mu(1-\mu)-\sigma^2\right], \tag{A2}$$

$$\alpha=\frac{\mu\beta}{1-\mu}, \tag{A3}$$

For a specific unit, the mean (μ) is a constant, equaling the total area proportion of the target land cover type, whereas the variance (σ^2) changes with different resolutions. When the spatial resolution is coarser in relation to the patch size of the target land cover type, the variance decreases. Though the abovementioned beta function was developed for the true abundances (f), it also applies to the estimated abundances ($\widehat{f}$) given their high similarity.

References

Adhikari, P., de Beurs, K.M., 2016. An evaluation of multiple land-cover data sets to estimate cropland area in West Africa. Int. J. Rem. Sens. 37, 5344–5364.
Atkinson, P.M., 1997. Mapping sub-pixel boundaries from remotely sensed images. Innovations in GIS. CRC Press, pp. 184–202.
Boschetti, L., Flasse, S.P., Brivio, P.A., 2004. Analysis of the conflict between omission and commission in low spatial resolution dichotomic thematic products: the Pareto Boundary. Rem. Sens. Environ. 91, 280–292.
Breiman, L., 2001. Random forests. Mach. Learn. 45, 5–32.
Breiman, L., 2002. Manual on Setting up, Using, and Understanding Random Forests V3. 1, vol. 1. Statistics Department University of California, Berkeley, CA, USA, pp. 3–42.
Bullock, E.L., Woodcock, C.E., Olofsson, P., 2020. Monitoring tropical forest degradation using spectral unmixing and Landsat time series analysis. Rem. Sens. Environ. 238, 110968.
Cao, S., Feng, J., Hu, Z., Li, Q., Wu, G., 2022. Improving estimation of urban land cover fractions with rigorous spatial endmember modeling. ISPRS J. Photogrammetry Remote Sens. 189, 36–49.
Card, D., 1982. Using known map category marginal frequencies to improve estimates of thematic map accuracy. Photogramm. Eng. Rem. Sens. 48.
Chen, Y., Ge, Y., Chen, Y., Jin, Y., An, R., 2018. Subpixel land cover mapping using multiscale spatial dependence. IEEE Trans. Geosci. Rem. Sens. 56, 5097–5106.
Cochran, W.G., 1977. Sampling Techniques. John Wiley & Sons.

Collins, J.B., Woodcock, C.E., 1999. Modeling the distribution of cover fraction of a geophysical field. In: Atkinson, P.M., Tate, N.J. (Eds.), Advances in Remote Sensing and GIS Analysis. John Wiley and Sons Ltd, Chichester, pp. 119–133.
Czaplewski, R.L., 1992. Misclassification bias in areal estimates. Photogramm. Eng. Rem. Sens. 58, 189–192.
Czaplewski, R.L., Catts, G.P., 1992. Calibration of remotely sensed proportion or area estimates for misclassification error. Rem. Sens. Environ. 39, 29–43.
Deng, C.B., Wu, C.S., 2012. BCI: a biophysical composition index for remote sensing of urban environments. Rem. Sens. Environ. 127, 247–259.
Fritz, S., See, L., McCallum, I., You, L., Bun, A., Moltchanova, E., Duerauer, M., Albrecht, F., Schill, C., Perger, C., Havlik, P., Mosnier, A., Thornton, P., Wood-Sichra, U., Herrero, M., Becker-Reshef, I., Justice, C., Hansen, M., Gong, P., Abdel Aziz, S., Cipriani, A., Cumani, R., Cecchi, G., Conchedda, G., Ferreira, S., Gomez, A., Haffani, M., Kayitakire, F., Malanding, J., Mueller, R., Newby, T., Nonguierma, A., Olusegun, A., Ortner, S., Rajak, D.R., Rocha, J., Schepaschenko, D., Schepaschenko, M., Terekhov, A., Tiangwa, A., Vancutsem, C., Vintrou, E., Wenbin, W., van der Velde, M., Dunwoody, A., Kraxner, F., Obersteiner, M., 2015. Mapping global cropland and field size. Global Change Biol. 21, 1980–1992.
Gallego, F.J., 2004. Remote sensing and land cover area estimation. Int. J. Rem. Sens. 25, 3019–3047.
Goodfellow, I., Bengio, Y., Courville, A., 2016. Deep Learning. MIT press, Cambridge.
Hansen, M.C., DeFries, R.S., Townshend, J.R.G., Carroll, M., Dimiceli, C., Sohlberg, R.A., 2003. Global percent tree cover at a spatial resolution of 500 meters: first results of the MODIS vegetation continuous fields algorithm. Earth Interact. 7, 1–15.
Hu, T.Y., Yang, J., Li, X.C., Gong, P., 2016. Mapping urban land use by using Landsat images and open social data. Rem. Sens. 8, 18.
Huete, A., Didan, K., Miura, T., Rodriguez, E.P., Gao, X., Ferreira, L.G., 2002. Overview of the radiometric and biophysical performance of the MODIS vegetation indices. Rem. Sens. Environ. 83, 195–213.
Huete, A.R., Liu, H.Q., Batchily, K., van Leeuwen, W., 1997. A comparison of vegetation indices over a global set of TM images for EOS-MODIS. Rem. Sens. Environ. 59, 440–451.
Keshava, N., Mustard, J.F., 2002. Spectral unmixing. IEEE Signal Process. Mag. 19, 44–57.
Key, J.R., 1994. The area coverage of geophysical fields as A function of sensor field-of-view. Rem. Sens. Environ. 48, 339–346.
King, L., Adusei, B., Stehman, S.V., Potapov, P.V., Song, X.-P., Krylov, A., Di Bella, C., Loveland, T.R., Johnson, D.M., Hansen, M.C., 2017. A multi-resolution approach to national-scale cultivated area estimation of soybean. Rem. Sens. Environ. 195, 13–29.
Lobell, D.B., Asner, G.P., 2004. Cropland distributions from temporal unmixing of MODIS data. Rem. Sens. Environ. 93, 412–422.
MacLachlan, A., Roberts, G., Biggs, E., Boruff, B., 2017. Subpixel land-cover classification for improved urban area estimates using Landsat. Int. J. Rem. Sens. 38, 5763–5792.
McRoberts, R., 2010. Probability- and model-based approaches to inference for proportion forest using satellite imagery as ancillary data. Rem. Sens. Environ. 114, 1017–1025.
Moody, A., Woodcock, C.E., 1994. SCALE-DEPENDENT errors in the estimation of land-cover proportions - implications for global land-cover datasets. Photogramm. Eng. Rem. Sens. 60, 585–594.
Olofsson, P., Foody, G.M., Herold, M., Stehman, S.V., Woodcock, C.E., Wulder, M.A., 2014. Good practices for estimating area and assessing accuracy of land change. Rem. Sens. Environ. 148, 42–57.
Ozdogan, M., Woodcock, C.E., 2006. Resolution dependent errors in remote sensing of cultivated areas. Rem. Sens. Environ. 103, 203–217.
Pan, Y., Li, L., Zhang, J., Liang, S., Zhu, X., Sulla-Menashe, D., 2012. Winter wheat area estimation from MODIS-EVI time series data using the Crop Proportion Phenology Index. Rem. Sens. Environ. 119, 232–242.
Pickens, A., Hansen, M., Hancher, M., Stehman, S., Tyukavina, A., Potapov, P., Marroquin, B., Sherani, Z., 2020. Mapping and sampling to characterize global inland water dynamics from 1999 to 2018 with full Landsat time-series. Rem. Sens. Environ. 243, 111792.
Pittman, K., Hansen, M.C., Becker-Reshef, I., Potapov, P.V., Justice, C.O., 2010. Estimating global cropland extent with multi-year MODIS data. Rem. Sens. 2, 1844–1863.
Potapov, P., Dempewolf, J., Talero, Y., Hansen, M., Stehman, S., Vargas, C., Rojas, E., Castillo, D., Mendoza, E., Calderón, A., Giudice, R., Malaga, N., Zutta, B., 2014. National satellite-based humid tropical forest change assessment in Peru in support of REDD+ implementation. Environ. Res. Lett. 9.
Powell, R.L., Roberts, D.A., Dennison, P.E., Hess, L.L., 2007. Sub-pixel mapping of urban land cover using multiple endmember spectral mixture analysis: manaus, Brazil. Rem. Sens. Environ. 106, 253–267.
Ridd, M.K., 1995. Exploring A V-I-S (Vegetation-Impervious surface-soil) model for urban ecosystem Analysis through remote-sensing - comparative anatomy for cities. Int. J. Rem. Sens. 16, 2165–2185.
Roberts, D.A., Gardner, M., Church, R., Ustin, S., Scheer, G., Green, R.O., 1998. Mapping chaparral in the Santa Monica Mountains using multiple endmember spectral mixture models. Rem. Sens. Environ. 65, 267–279.
Sannier, C., McRoberts, R., Fichet, L.-V., Makaga, E., 2013. Using the regression estimator with Landsat data to estimate proportion forest cover and net proportion deforestation in Gabon. Rem. Sens. Environ. 151.
Somers, B., Asner, G.P., Tits, L., Coppin, P., 2011. Endmember variability in spectral mixture analysis: a review. Rem. Sens. Environ. 115, 1603–1616.
Stehman, S.V., 2009. Model-assisted estimation as a unifying framework for estimating the area of land cover and land-cover change from remote sensing. Rem. Sens. Environ. 113, 2455–2462.
Stehman, S.V., 2013. Estimating area from an accuracy assessment error matrix. Rem. Sens. Environ. 132, 202–211.
Stehman, S.V., Foody, G.M., 2019. Key issues in rigorous accuracy assessment of land cover products. Rem. Sens. Environ. 231, 111199.
Tang, H., Zhou, Q., Liu, J., Li, Z., Wu, W., 2016. Wheat Mapping Using High Resolution Remote Sensing Data. Science Press, Beijing, China.
Turubanova, S., Potapov, P., Tyukavina, A., Hansen, M., 2018. Ongoing primary forest loss in Brazil, Democratic Republic of the Congo, and Indonesia. Environ. Res. Lett. 13.
Waldner, F., Defourny, P., 2017. Where can pixel counting area estimates meet user-defined accuracy requirements? Int. J. Appl. Earth Obs. Geoinf. 60, 1–10.
Wang, Q., Shi, W., Atkinson, P.M., 2014. Sub-pixel mapping of remote sensing images based on radial basis function interpolation. ISPRS J. Photogramm. Remote Sens. 92, 1–15.
Wang, Q., Zhang, C., Atkinson, P.M., 2020. Sub-pixel mapping with point constraints. Rem. Sens. Environ. 244, 111817.
Wang, Q., Zhang, C., Tong, X., Atkinson, P., 2020. General solution to reduce the point spread function effect in subpixel mapping. Rem. Sens. Environ. 251, 112054.
Weng, Q.H., 2012. Remote sensing of impervious surfaces in the urban areas: requirements, methods, and trends. Rem. Sens. Environ. 117, 34–49.
Wu, C.S., 2004. Normalized spectral mixture analysis for monitoring urban composition using ETM plus imagery. Rem. Sens. Environ. 93, 480–492.
Wu, C.S., Murray, A.T., 2003. Estimating impervious surface distribution by spectral mixture analysis. Rem. Sens. Environ. 84, 493–505.
Xu, F., Cao, X., Chen, X.H., Somers, B., 2019. Mapping impervious surface fractions using automated Fisher transformed unmixing. Rem. Sens. Environ. 232, 14.
Xu, F., Somers, B., 2021. Unmixing-based Sentinel-2 downscaling for urban land cover mapping. ISPRS J. Photogrammetry Remote Sens. 171, 133–154.
Zare, A., Ho, K.C., 2014. Endmember variability in hyperspectral analysis. IEEE Signal Process. Mag. 31, 95–104.
Zha, Y., Gao, J., Ni, S., 2003. Use of normalized difference built-up index in automatically mapping urban areas from TM imagery. Int. J. Rem. Sens. 24, 583–594.
Zhang, C., Ma, L., Chen, J., Rao, Y., Zhou, Y., Chen, X., 2019. Assessing the impact of endmember variability on linear Spectral Mixture Analysis (LSMA): a theoretical and simulation analysis. Rem. Sens. Environ. 235.
Zhang, Y.S., Odeh, I.O.A., Han, C.F., 2009. Bi-temporal characterization of land surface temperature in relation to impervious surface area, NDVI and NDBI, using a sub-pixel image analysis. Int. J. Appl. Earth Obs. Geoinf. 11, 256–264.
Zhong, Y., Wu, Y., Xu, X., Zhang, L., 2015. An adaptive subpixel mapping method based on MAP model and class determination strategy for hyperspectral remote sensing imagery. IEEE Trans. Geosci. Remote. Sens. 53, 1411–1426.